


# A convenient setup for laser-induced fluorescence imaging of both CO and CO<sub>2</sub> during catalytic CO oxidation

Jianfeng Zhou<sup>1</sup>  · S. Pfaff<sup>1</sup> · E. Lundgren<sup>2</sup> · J. Zetterberg<sup>1</sup>

Received: 24 November 2016 / Accepted: 20 February 2017 / Published online: 10 March 2017  
© The Author(s) 2017. This article is published with open access at Springerlink.com

**Abstract** In-situ knowledge of the gas composition close to a catalyst is essential for a better understanding of the gas–surface interaction. With planar laser-induced fluorescence (PLIF), the gas distribution around an operating catalyst can be visualized with high spatial and temporal resolution, in a non-intrusive manner. We report on a convenient setup using a nanosecond YAG-Dye laser system together with a broadband mid-infrared optical parametric oscillator (OPO) for imaging both CO and CO<sub>2</sub> over a Pd(100) catalyst during catalytic CO oxidation, compare it to previously used systems, and show examples of its capabilities.

## 1 Introduction

Catalysis plays an important role in our daily life. Approximately 90% of all chemicals and materials around us are produced using catalysis at one stage or another [1]. In addition to this, catalysis is used to reduce emissions for a more sustainable society. For example, the three-way catalyst is used in almost every gasoline-fueled vehicle to clean the exhaust gases from harmful species such as CO, NO<sub>x</sub>, and hydrocarbons. CO oxidation, being an important model reaction, has been studied intensively for many decades

[2]. The reaction process is well known under ultra-high vacuum (UHV) conditions where gas flows and gas distribution around a sample are often neglected. However, the number of molecules interacting with the catalyst surface increases significantly at elevated pressures, and as a result, a change in the gas composition close to the surface may lead to a change of the surface structure [3, 4]. Therefore, it is essential to obtain in-situ knowledge of the gas composition close to an operating catalyst to achieve a better understanding of the gas–surface interaction.

Conventional gas analytical tools such as mass spectrometry (MS), gas chromatography (GC), and Fourier transform infrared spectrometry (FTIR) are often used to analyze gases from the outlet of a reactor. These techniques have the benefit of measuring several species simultaneously, but they suffer from a time delay or poor temporal resolution, and are not capable to spatially resolve the gas composition around a sample. Although capillary sampling techniques can provide spatially resolved concentration profiles inside reactors [5], it cannot deliver two-dimensional measurements to follow dynamic changes in the gas phase on a sub-second scale, and the intrusive nature of the probe may introduce errors in data interpretation.

As an in-situ and non-invasive gas detection technique with high spatial and temporal resolution, planar laser-induced fluorescence (PLIF) has been widely used in the combustion community for flame studies [6–8], but much less applied in the catalyst community [9]. In earlier studies during the 1990s, LIF has been used to study the OH formation close to a Pt catalyst during the H<sub>2</sub> oxidation [10–14], the distribution of OH desorbed from a Pt catalyst during catalytic water formation reaction [15], and the formaldehyde distribution above a platinum plate during catalytic combustion of methanol/air mixtures [16]. However, in the 2000s, there were

---

**Electronic supplementary material** The online version of this article (doi:10.1007/s00340-017-6681-3) contains supplementary material, which is available to authorized users.

---

✉ Jianfeng Zhou  
Jianfeng.zhou@forbrf.lth.se

<sup>1</sup> Division of Combustion Physics, Lund University, 221 00 Lund, Sweden

<sup>2</sup> Division of Synchrotron Radiation Research, Lund University, 221 00 Lund, Sweden

very limited works related to catalysis studies, two of which are the studies of OH during the gas phase combustion of fuel-lean methane/air pre-mixtures over Pt [17], and formaldehyde over supported Rh catalysts for partial oxidation of methane in exhaust gas diluted reaction mixtures [18]. Over the past few years, applications of the technique have been largely extended to study the distribution of CO<sub>2</sub> and/or CO over model catalysts during CO oxidation [19–25], hydrogen-assisted NH<sub>3</sub> oxidation above a Ag/Al<sub>2</sub>O<sub>3</sub> powder catalyst [23], as well as catalytic reduction of NO by hydrogen to ammonia over a Pt/Al<sub>2</sub>O<sub>3</sub> catalyst [26]. All of these studies have demonstrated PLIF as a powerful complimentary tool to conventional tools, such as MS, for studies of gas phase in catalysis.

In previous works by Blomberg et al. [20], the detection of CO and CO<sub>2</sub> from CO oxidation was carried out separately using two large laser systems. The CO PLIF was performed using a picosecond laser system consisting of a mode-locked Nd:YAG laser with an external amplifier and an optical parametric generator, yielding a broadband UV beam. And the CO<sub>2</sub> PLIF was performed using a nanosecond laser system consisting of a Nd:YAG laser, a dye laser, and a mixing unit, generating a tunable narrowband infrared laser beam.

Here we report a convenient setup using a nanosecond YAG-Dye laser system together with a broadband mid-infrared optical parametric oscillator (OPO) for imaging both CO and CO<sub>2</sub>. CO is detected via the visible-wavelength fluorescence (450–660 nm) of the B<sup>1</sup>Σ<sup>+</sup>→A<sup>1</sup>Π transition in the Angstrom bands by nanosecond two-photon excitation of the X<sup>1</sup>Σ<sup>+</sup>→B<sup>1</sup>Σ<sup>+</sup> transition at 230.1 nm [27, 28], while CO<sub>2</sub> is detected via the mid-infrared fluorescence from the fundamental band ~4.3 μm by broadband excitation at ~2.7 μm. Excitation at 2.7 μm is chosen as an optimized scheme for the current setup, because it provides relatively strong absorption cross section, while the laser absorption by the air along the beam path is not so severe. Other excitation schemes for CO<sub>2</sub> PLIF detection can be found in [29–33]. As a proof of concept, quantitative measurements of both CO and CO<sub>2</sub> over a Pd catalyst during catalytic CO oxidation have been carried out to demonstrate the high spatial and temporal resolution of the two techniques for studies of gas phase in catalysis. Comparisons between the picosecond and nanosecond excitation approaches for CO detection, and between the narrowband and broadband excitation approaches for CO<sub>2</sub> detection, will be presented. The quenching effect on the signal calibration for both CO and CO<sub>2</sub> will also be discussed.

## 2 Experiment

### 2.1 Laser-induced fluorescence

The optical setup to perform measurements of CO and CO<sub>2</sub> is shown in Fig. 1. An injection seeded Nd:YAG laser (Continuum, Powerlite DLS 8010) operating at second harmonic (532 nm, 800 mJ/pulse, 10 Hz) was used to pump the Dye laser (Continuum, Vista) running on R610 dye (Exiton), with ethanol as solvent, which produced laser radiation of around 150 mJ at 587.2 nm with a linewidth specified to 0.05 cm<sup>-1</sup>. This fundamental dye output was then frequency doubled by a BBO crystal (Continuum, Vista FX) to obtain a UV beam of around 30 mJ/pulse at 293.6 nm. This UV beam was mixed in a second BBO crystal (Continuum, Vista FX) with the residual 1064 nm beam from the Nd:YAG laser, generating laser pulses at 230.1 nm of energy ~9 mJ and pulse width ~5 ns. The 230.1-nm beam was steered by three UV-fused silica prisms, shaped into a thin laser sheet of

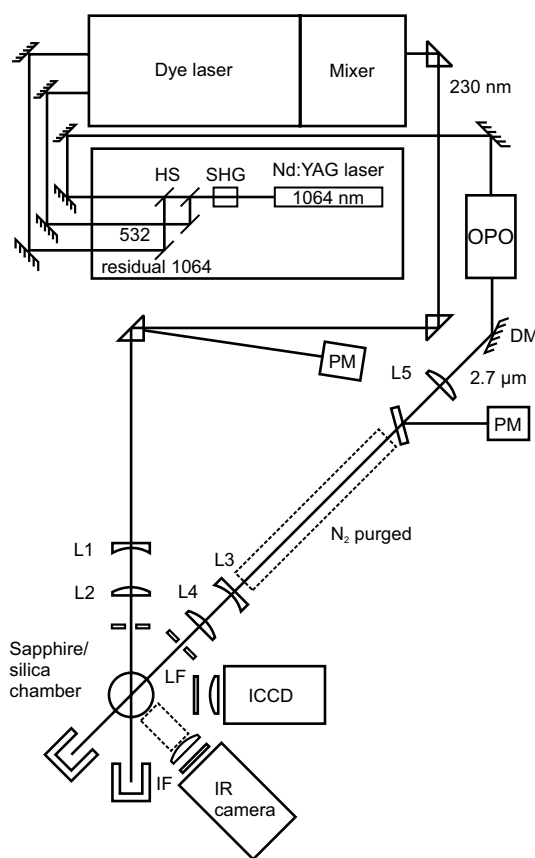


**Fig. 1** Schematic of the optical setup. SHG, second harmonic generator; HS, harmonics separators; L1 UVFS lens,  $f = -40$  mm; L2 UVFS lens,  $f = 150$  mm; L3 CaF<sub>2</sub> lens,  $f = -40$  mm; L4 CaF<sub>2</sub> lens,  $f = 100$  mm; L5 CaF<sub>2</sub> lens,  $f = 500$  mm; DM dichroic mirror, PM power meter, IF interference filter, LF long-pass filter; dashed boxes indicate the N<sub>2</sub> purged region

~6 mm height by a cylindrical and a spherical lens,  $f = -40$  mm and  $f = 150$  mm, respectively, and sent through the silica chamber just above the catalyst sample. The laser sheet had energy of ~2.5 mJ in front of the chamber, mainly due to energy losses from the optics and edge cutting by the aperture. The reflected 230.1-nm beam from one of the prisms was measured by a power meter (Gentec-EO, Maestro) to keep track of shot-to-shot variation in the laser pulse energy during measurement.

The CO fluorescence was imaged by an ICCD camera (Princeton Instruments, PIMAX 3) using an objective (Nikor  $f = 50$  mm,  $f/1.2$ ) with a 31-mm extension ring mounted on the camera. The intensifier gate was set to 250 ns, which is much longer than the collision-free lifetime (68 ns) of the  $B^1\Sigma^+$  fluorescence [34]. Images were acquired at a 10-Hz repetition rate. The CCD chip was hardware-binned  $2 \times 2$  to increase the image acquisition rate as well as the signal-to-noise ratio (SNR). A long-pass filter (GG455, Schott) was applied to suppress the scattering and fluorescence from the fused silica chamber below 455 nm.

To switch the laser output from UV to mid-IR for CO<sub>2</sub> detection, the second harmonic generator (SHG) crystal and the harmonics separators (HS) were removed from the YAG laser. The fundamental 1064-nm laser beam with ~350 mJ/pulse from the YAG laser was used to pump an IR-OPO (GWU, versaScan-L 1064), generating a signal beam ~1.7  $\mu\text{m}$  and an idler beam at 2.7  $\mu\text{m}$ , with ~8 mJ/pulse and ~7 mJ/pulse, respectively. Both the signal and idler beams have pulse width of ~5 ns. The idler beam was separated from the signal beam by a dichroic mirror (HR at 2.7  $\mu\text{m}$ ), and formed into a thin laser sheet of ~6 mm height by a cylindrical and two spherical lenses,  $f = -40$  mm,  $f = 100$  mm, and  $f = 500$  mm, respectively, and sent through the sapphire chamber just above the catalyst. The idler beam had energy of ~3 mJ in front of the chamber. A CaF<sub>2</sub> window in the beam path was used to reflect ~10% of the laser energy to keep track of shot-to-shot variation with a power meter.

The CO<sub>2</sub> fluorescence was imaged by a liquid-nitrogen-cooled,  $256 \times 256$  InSb IR camera (Santa Barbara Focal Plane, SBF LP134) using a CaF<sub>2</sub> lens ( $f = 50$  mm,  $f/2.3$ ). A cold interference filter inside the camera, centered at 4.26  $\mu\text{m}$  and with FWHM of 200 nm, was used to suppress the strong thermal background. As the radiative lifetime of the IR-transition is rather long ~100  $\mu\text{s}$  [29], the exposure time was set to 30  $\mu\text{s}$  to discriminate background and favor fluorescence signal, and a time delay of 10  $\mu\text{s}$  relative to the Q-switch of the YAG laser was used to avoid scattering from the laser and time jitter. As the thermal background was continuously varying during the experiments, the camera was triggered at 20 Hz, via a pulse generator (BNC, Model 575), with every second exposure measuring the background, which was to be subtracted afterwards. A

more detailed description of this detection scheme can be referred to [19]. To reduce laser energy attenuation along the beam path and fluorescence signal loss between the cell and the IR camera, purging of N<sub>2</sub> was applied during measurements.

## 2.2 Sample and catalysis reactor

The sample investigated was a Pd single crystal with diameter of 8 mm, thickness of 2 mm and a (100) surface orientation. A fused silica cylindrical chamber with diameter of 30 mm and height of 25 mm was used for the CO measurements, while a sapphire one of the same dimensions for the CO<sub>2</sub> measurements. Gases were supplied to the reactor by individual mass flow controllers (Bronkhorst EL-FLOW), and the gas pressure in the reactor was controlled by a digital pressure controller (Bronkhorst EL-PRESS). The gas composition in the reactor was measured by a quadrupole mass spectrometer (Pfeiffer, QME 220) connected to the outlet of the reactor with an automated leak valve. The sample was heated by a boralelectric heater, the temperature of which was measured by a type D thermocouple. When the sample was heated at a slow speed of ~15 °C/min, the temperature of the sample was assumed to be the same as the sample heater.

## 3 Results and discussions

To examine the CO and CO<sub>2</sub> absorption behaviors to the corresponding excitation laser sources, excitation scans for both CO and CO<sub>2</sub> have been performed, as shown in Fig. 2. For the CO excitation scan, 4% CO was mixed in Ar at room temperature and a pressure of 150 mbar, while for the CO<sub>2</sub> excitation scan, 4% CO<sub>2</sub> was mixed in Ar at the same temperature and pressure. Before each measurement, the chamber was pumped down to a very low pressure (~1 mbar) and then purged with the measured gases. The purging lasted for long enough time (~5 min) to ensure that there is no or negligible amount of residual gases in the chamber. In Fig. 2, a smoothing of five consecutive data points has been applied to both scans to reduce noise due to shot-to-shot laser energy fluctuation.

As can be seen in Fig. 2a, a high-resolution CO spectrum showing the Q-branch of the  $B^1\Sigma^+(v' = 0) \rightarrow A^1\Pi(v'' = 0)$  transition is obtained thanks to the narrowband UV beam. By convoluting a variety of laser profiles (with assumed Gaussian shape) and a simulated CO absorption spectrum (at 296 K and 150 mbar), and comparing the convoluted spectra with the measured CO excitation scan, the full-width of half maximum (FWHM) of the UV laser is estimated to ~0.5  $\text{cm}^{-1}$  (0.0026 nm). In contrast to CO, the CO<sub>2</sub> spectrum in Fig. 2 b exhibits a very broad feature due

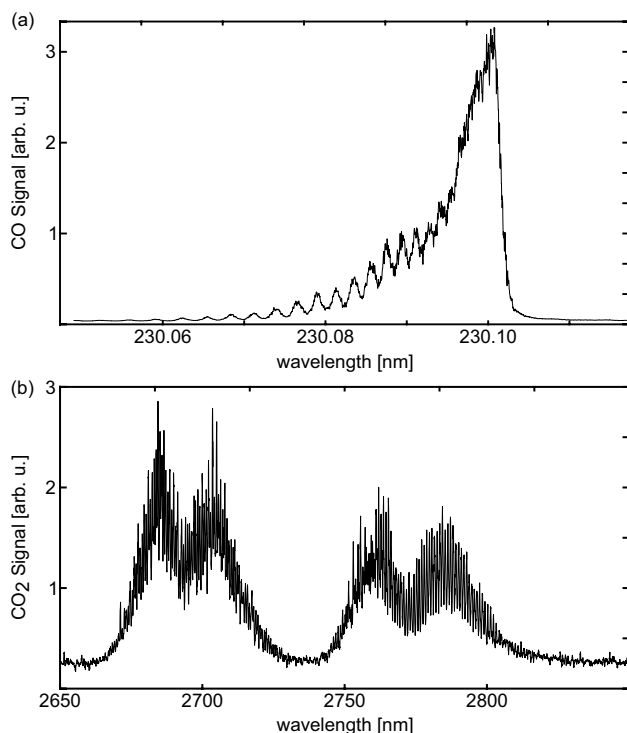


**Fig. 2** Excitation spectrum of CO (a) and CO<sub>2</sub> (b) at room temperature and 150 mbar

to the broadband laser from the IR-OPO. In a similar manner as above, the full-width of half maximum (FWHM) of the IR laser is estimated to  $\sim 10 \text{ cm}^{-1}$  (7.3 nm). Thus, the linewidth of this laser covers a number of ro-vibrational lines in the  $(00^0_0) \rightarrow (10^0_0)$  transition of CO<sub>2</sub>. It is worth noting that the linewidth of the laser from this IR-OPO has strong wavelength dependence. At wavelength  $\sim 3 \mu\text{m}$ , the linewidth was previously measured to  $\sim 5 \text{ cm}^{-1}$  using an IR grating and an IR camera [35].

For quantitative PLIF measurements of CO and CO<sub>2</sub>, the concentration dependence on the fluorescence signal for both CO and CO<sub>2</sub> was investigated by varying the partial pressure of CO and CO<sub>2</sub> in Ar separately at non-reacting conditions. For non-reacting conditions, the sample was heated at the same total chamber pressure and gas flow rates as for reacting conditions. In this way, the temperature gradient of the gases close to the sample surface will be the same for non-reacting and reacting conditions. Figure 3 shows the concentration dependence of the fluorescence signal for both CO and CO<sub>2</sub>, at 300 °C (sample temperature), 150 mbar total chamber pressure, and 100 mL<sub>n</sub>/min total flow rate. Each point is an average of 200 laser shots (corresponds to an acquisition time of 20 s), and the standard deviation of the 200 measurements is presented by the error bars. For both CO and CO<sub>2</sub>, the laser energies used were non-saturating. The CO signal shows

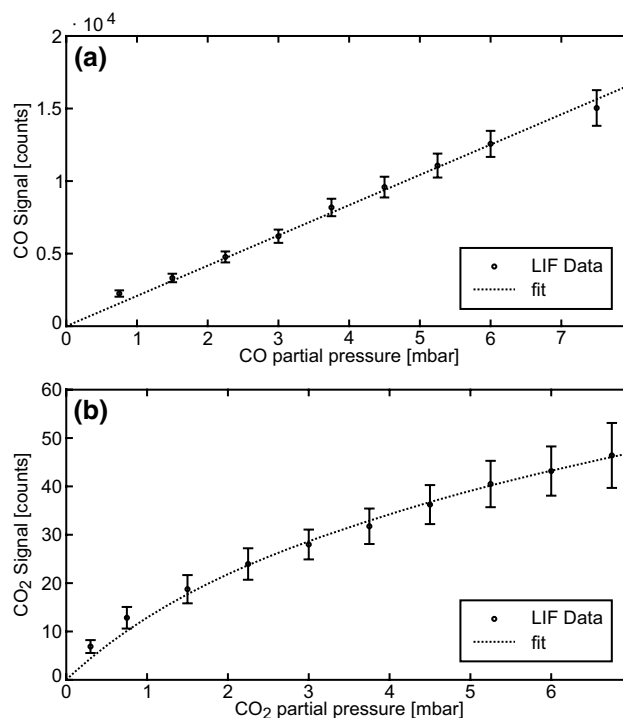


**Fig. 3** Concentration dependence of the fluorescence signal for CO (a) and CO<sub>2</sub> (b), at 300 °C and 150 mbar

linear concentration dependence. With a linear fitting, the single-shot detection limit of CO is estimated to 0.5 mbar (SNR = 1). In contrast to CO, the CO<sub>2</sub> curve is slightly bent towards higher concentrations due to self-absorption effect inside the chamber. The CO<sub>2</sub> signal is fitted with a function taking into account the self-absorption, and the single-shot detection limit of CO<sub>2</sub> is estimated to 0.1 mbar (SNR = 1).

It is worth noting that the CO<sub>2</sub> measured at reacting conditions is mainly localized in a hemispherical cloud above the sample, and the size of this cloud is much smaller than that of the chamber. Using the Beer–Lambert Law in Eq. (1),

$$\frac{I}{I_0} = \exp\left(-\frac{qPl}{kT}\sigma_v\right) = \exp(-Nl\sigma_v), \quad (1)$$

where  $I$  is the intensity after the path,  $I_0$  is the initial intensity before the path,  $\sigma_v$  is the IR cross section,  $q$  is the mole fraction,  $P$  is the pressure,  $T$  is the temperature,  $k$  is Boltzmann's constant,  $l$  is the path length, and  $N$  is the number of absorbers; the mass path  $Nl$  is estimated to be a factor of 4 smaller for reacting conditions than non-reacting conditions, given that the diameters of the sample and the chamber are 8 and 30 mm, respectively. Furthermore, the maximum partial pressure of CO<sub>2</sub> at reacting conditions is kept below 6 mbar. Therefore, the self-absorption effect is considered negligible for the CO<sub>2</sub> measurements at reacting conditions.

To show the capabilities of the current setup, two separate PLIF measurements were performed during CO oxidation over a Pd(100) single-crystal catalyst, one for CO and the other for CO<sub>2</sub>. Figure 4 summarizes the measurement results. The two measurements were performed using similar heating current ramp speed; the current was ramped from 0.65 to 1.15 A for CO, and from 0.6 to 1.2 A for CO<sub>2</sub>, both in 600 s. For comparison, the temperature range from 200 to 346 °C is shown. Both measurements were performed at flows of 4 mL<sub>n</sub>/min CO, 4 mL<sub>n</sub>/min O<sub>2</sub>, and 92 mL<sub>n</sub>/min Ar at 150 mbar total pressure (corresponding to initial partial pressures of 6 mbar of CO, 6 mbar of O<sub>2</sub>, and 138 mbar of Ar). In both cases, the vertical laser sheet was positioned above the sample (indicated by the white rectangle), and a small region (indicated by the dashed box) in the bottom of the laser sheet was averaged to evaluate the LIF signals close to the sample surface. The spatial resolution for CO is 40 μm/pixel, and for CO<sub>2</sub> 80 μm/pixel. The temporal resolution for both CO and CO<sub>2</sub> PLIF measurements is 0.1 s, but the PLIF images presented are 10-shot averaged, giving a temporal resolution of 1 s.

At low temperature 253 °C, a homogeneous CO distribution can be seen in Fig. 4a. This corresponds to the CO<sub>2</sub> PLIF image in Fig. 4g showing very little CO<sub>2</sub> produced. Both the CO and CO<sub>2</sub> PLIF images indicate that the sample is inactive. As the temperature increases, the partial pressure of CO drops and the partial pressure of CO<sub>2</sub> increases steadily, as shown in the MS in Fig. 4e and the LIF trends in Fig. 4d, f. When the sample ignites (the highly active phase of the catalytic reaction initiates), the gradient of the CO

and CO<sub>2</sub> concentrations above the sample changes significantly, as can be seen in Fig. 4b, h, respectively. When the sample is highly active, a clear depletion of CO and a formation of CO<sub>2</sub> above the sample can be seen in Fig. 4c, i, respectively. From both the MS and LIF trends, the CO and CO<sub>2</sub> concentrations stabilize immediately (less than 1 s) after the ignition of the sample. This indicates that the reaction has reached the mass transfer limited (MTL) regime, i.e., the reaction is mass transfer limited by the ability of CO molecules diffusing and reaching onto the surface. In the MTL regime, the gas distribution over the sample is not homogeneous, and a decrease of ~70% for the CO concentration close to the sample is measured by PLIF, compared to only ~20% observed by the MS located at the gas outlet of the chamber. This significant difference can be explained by the fact that the MS is sampling gases far away from the sample surface, in this case about 30 mm. It is worth pointing out that the shift of the CO and CO<sub>2</sub> cloud to the right of the sample is due to the gas flow.

Since this work presents a detection approach each for CO and CO<sub>2</sub> in catalysis studies, it is interesting to compare them with other approaches used in previous works. For CO detection, the nanosecond excitation approach in this work is compared to the picosecond excitation approach used in [20]. The benefit of using a picosecond pulse is that it can provide high peak power beneficial for the two-photon excitation process, and lower C<sub>2</sub> interference from flames, compared to using a nanosecond pulse [36]. Since C<sub>2</sub> interference is not of concern in this work, it is mostly interesting to compare the CO detection limit and laser

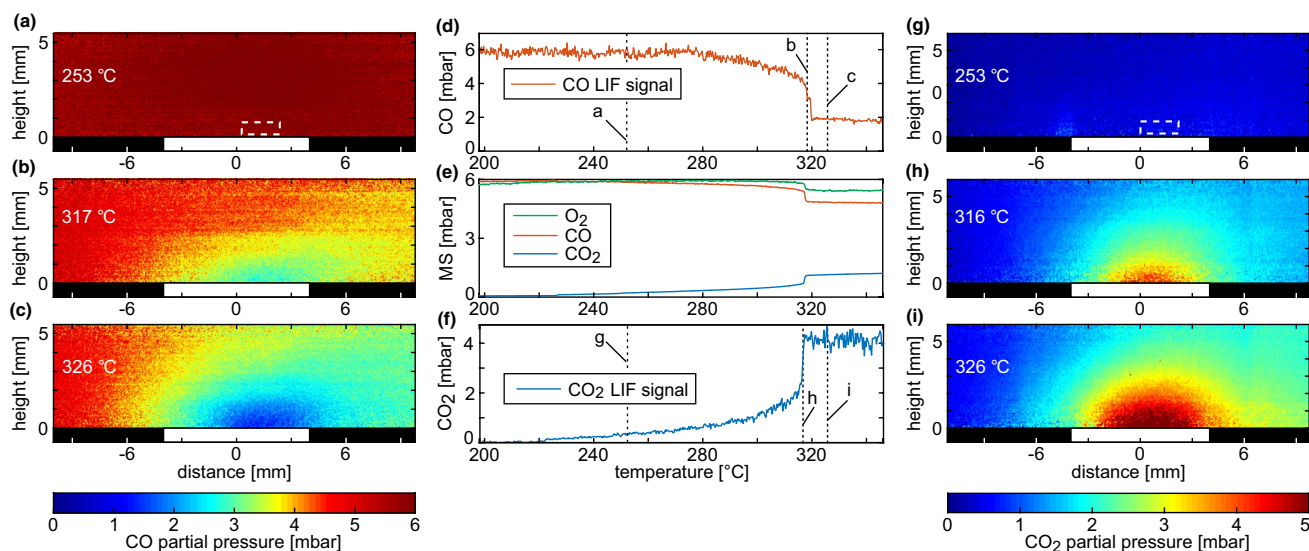


**Fig. 4** PLIF imaging of both CO and CO<sub>2</sub> during CO oxidation over a Pd(100) single crystal (*white rectangular*). **a–c** show CO PLIF images; **d** shows the average CO PLIF signal; **e** shows the MS trends of CO, O<sub>2</sub> and CO<sub>2</sub>; **f** shows the average CO<sub>2</sub> PLIF signal; **g–i** show

CO<sub>2</sub> PLIF images; the *dashed boxes* indicate the region used to evaluate the PLIF signals. All PLIF images are 10 laser shot averaged, representing acquisition time 1 s

**Table 1** Comparison of CO PLIF between nanosecond and picosecond excitation approaches

| CO PLIF    | Excitation wave-length (nm) | Linewidth FWHM (cm <sup>-1</sup> ) | Linewidth FWHM (nm) | Pulse Energy (mJ) | Pulse length | Gate (ns) | Spatial resolution (μm) | Temporal resolution (s) |
|------------|-----------------------------|------------------------------------|---------------------|-------------------|--------------|-----------|-------------------------|-------------------------|
| Nanosecond | 230.1                       | 0.5                                | 0.0026              | 9                 | 5 ns         | 250       | 40                      | 0.1                     |
| Picosecond | 230.1                       | 5                                  | 0.026               | 0.4               | 80 ps        | 30        | 60                      | 0.1                     |

**Table 2** Comparison of CO<sub>2</sub> PLIF between broadband and narrowband excitation approaches

| CO <sub>2</sub> PLIF | Excitation wave-length (μm) | Linewidth FWHM (cm <sup>-1</sup> ) | Linewidth FWHM (nm) | Pulse Energy (mJ) | Pulse length (ns) | Gate (μs) | Spatial resolution (μm) | Temporal resolution (s) |
|----------------------|-----------------------------|------------------------------------|---------------------|-------------------|-------------------|-----------|-------------------------|-------------------------|
| Broadband            | 2.7                         | 10                                 | 7.3                 | 7                 | 5                 | 30        | 80                      | 0.1                     |
| Narrowband           | 2.7                         | 0.025                              | 0.018               | 4                 | 5                 | 20        | 70                      | 0.1                     |

shot-to-shot stability. For CO<sub>2</sub> detection, the broadband excitation approach in this work is compared to the narrowband excitation approach used in [23]. The comparison between them will be focused on their CO<sub>2</sub> detection limits. Tables 1 and 2 summarize the key parameters for the comparisons between the nanosecond and the picosecond excitation approaches for CO detection, and between the broadband and the narrowband excitation approaches for CO<sub>2</sub> detection. In each case, the two approaches employed almost the same detection optics (e.g., camera, objective, extension ring, and filter), which makes the comparisons more feasible.

For CO detection, a SNR of 3 with a standard deviation of 34% (for 10 laser shots) was measured for a CO partial pressure of 5 mbar at a total pressure of 100 mbar (in Ar) and 150 °C, using the picosecond excitation approach [20]. Based on the CO concentration dependence study in [20], the single-shot CO detection limit can be estimated to be around 2 mbar. In this work, the nanosecond excitation approach gives a lower single-shot detection limit of 0.5 mbar at similar conditions (150 mbar and 300 °C). Compared to the picosecond approach, the nanosecond excitation approach also gives smaller standard deviation within the same range of time, thus better laser shot-to-shot stability. For CO<sub>2</sub> detection, the detection limit of CO<sub>2</sub> was measured to 0.1 mbar at 300 °C and 150 mbar, using the narrowband excitation approach [23]. In this work, the broadband excitation approach gives a similar detection limit under the same conditions (150 mbar and 300 °C). However, the broadband excitation approach utilizes a small IR-OPO instead of a dye laser and a mixing unit used by the narrowband excitation approach, thus has the advantages of being more compact and convenient to use.

To evaluate the quenching effects on the calibrations of the CO and CO<sub>2</sub> PLIF signal and to compensate for it

**Table 3** Quenching effect on normalized CO and CO<sub>2</sub> PLIF signals. The total pressure is 150 mbar with Ar used as buffer gas

| Fluorescing gases | 6 mbar CO              |                       | 3 mbar CO <sub>2</sub> |                       |
|-------------------|------------------------|-----------------------|------------------------|-----------------------|
| Quencher gases    | 6 mbar CO <sub>2</sub> | 6 mbar O <sub>2</sub> | 6 mbar CO              | 6 mbar O <sub>2</sub> |
| 22 °C             | 0.88                   | 0.88                  | 0.75                   | 0.98                  |

to a certain extent, the PLIF signals with and without the quencher gases were recorded at room temperature. The results are shown in Table 3, where the values are normalized, i.e., the LIF signal with a quencher gas was divided by the LIF signal without a quencher gas. Note that Ar is not considered as a quencher gas here and was used as a buffer gas to keep the total pressure at 150 mbar, which is similar to the reacting conditions above.

As quenching is temperature dependent, the LIF signal at higher temperatures is evaluated using Eq. (2–5),

$$S_{\text{LIF}} = \eta_c E g f(T) \sigma_0 N \phi, \quad (2)$$

$$\phi = \frac{A}{A + \sum_i Q_i} \propto \frac{1}{\sum_i Q_i}, \quad (3)$$

$$Q_i = q_i p_i \propto \frac{\sigma_i^2 p_i}{\sqrt{T}}, \quad (4)$$

$$S_{\text{LIF}} \propto \frac{1}{\sum_i \sigma_i^2 p_i} \sqrt{T} f(T), \quad (5)$$

where  $S_{\text{LIF}}$  is the fluorescent intensity,  $\eta_c$  is the collection efficiency,  $E$  is the laser energy,  $g$  is a function that describes the spectral overlap between the laser and the absorption spectral lineshape,  $f(T)$  is the Boltzmann distribution,  $\sigma_0$  is the absorption cross section,  $N$  is the number

density of the absorber,  $\phi$  is the fluorescence quantum yield,  $Q_i$  is the quenching rate,  $q_i$  is the quenching rate coefficient,  $p_i$  is the partial pressure for species  $i$ ,  $\sigma_i$  is the quenching cross section, and Eq. (3) assumes that the spontaneous emission rate is far less than the quenching rate. Assuming the quenching cross sections in Eq. (5) are temperature independent over a small temperature range (300 K) for both CO [37] and CO<sub>2</sub>, the normalized PLIF signal will be independent of temperature. This means that the decrease of the LIF signal due to quenching is the same for different temperatures.

From Table 3, it can be seen that for CO, the quenching from O<sub>2</sub> and CO<sub>2</sub> was found to be similar, e.g., 6 mbar of each O<sub>2</sub> and CO<sub>2</sub> decrease the CO signal by 12%. And for CO<sub>2</sub>, the quenching from O<sub>2</sub> was found to be very small, e.g., 6 mbar O<sub>2</sub> only decreases the CO<sub>2</sub> signal by 2%, while the quenching from CO was found to be relatively strong, e.g., 6 mbar CO can reduce the CO<sub>2</sub> signal by 25%. To estimate the maximum deviation on the LIF signal calibration in Fig. 4 introduced by quenching, the reaction can be separated into two parts for the discussion, before and after ignition. Before ignition, the majority of gases in the cell (and close to the sample) are CO and O<sub>2</sub>. Therefore, the quenching is small for the CO signal and a maximum deviation of 12% is estimated due to the presence of 6 mbar O<sub>2</sub>. In contrast, the quenching is much stronger for the CO<sub>2</sub> signal and a maximum deviation of 25% is estimated due to the presence of 6 mbar of each CO and O<sub>2</sub>. After ignition, nearly all CO molecules reaching onto the surface are converted into CO<sub>2</sub>; thus, the majority of gases close to the sample are CO<sub>2</sub> and O<sub>2</sub>. As a result, the quenching for the CO<sub>2</sub> signal close to the sample is considered negligible. In contrast, the quenching for the CO signal close to the sample is much stronger, and has therefore been taken into account. After the correction for quenching, we obtained a good match between the CO and CO<sub>2</sub> profiles close to the sample when the reaction is in the highly active phase, i.e., around 2 mbar of CO and 4 mbar of CO<sub>2</sub>.

## 4 Conclusions

In this work, we have reported a convenient setup for LIF imaging of both CO and CO<sub>2</sub> from catalytic CO oxidation above a Pd(100) single-crystal catalyst. Both approaches for the CO and CO<sub>2</sub> detection are shown to have advantages over the previously used approaches. For CO detection, the nanosecond excitation approach presented in the current work gives lower detection limit and better shot-to-shot stability under similar conditions, compared to the picosecond excitation approach in the literature. For CO<sub>2</sub> detection, the broadband excitation approach with an IR-OPO reported here gives the same detection limit as the narrowband

excitation approach used in our previous work, but shows the merit of compactness and convenience. Simultaneous measurement of CO and CO<sub>2</sub> will be worth trying in future work using part of the residual 1064 beam from the YAG laser (another part for the UV mixing) to pump the IR-OPO. This will have distinct advantages over separate measurements for detection of CO and CO<sub>2</sub> in catalytic reactions, where the relation between the CO and CO<sub>2</sub> concentrations is not directly correlated, compared to the case in CO oxidation.

**Acknowledgements** This work was financially supported by the Knut and Alice Wallenberg Foundation, the Royal Physiographic Society of Lund, and the Swedish Research Council.

**Open Access** This article is distributed under the terms of the Creative Commons Attribution 4.0 International License (<http://creativecommons.org/licenses/by/4.0/>), which permits unrestricted use, distribution, and reproduction in any medium, provided you give appropriate credit to the original author(s) and the source, provide a link to the Creative Commons license, and indicate if changes were made.

## References

1. M. Bowker, *The basis and applications of heterogeneous catalysis* (Oxford University Press Inc., New York, 1998)
2. G. Ertl, H. Knözinger, J. Weitkamp, *Handbook of heterogeneous catalysis* (VCH, Weinheim, 2008)
3. F. Gao, S.M. McClure, Y. Cai, K.K. Gath, Y. Wang, M.S. Chen, Q.L. Guo, D.W. Goodman, *Surf. Sci.* **603**, 65 (2009)
4. J. Gustafson, M. Shipilin, C. Zhang, A. Stierle, U. Hejral, U. Ruett, O. Gutowski, P.-A. Carlsson, M. Skoglundh, E. Lundgren, *Science* **343**, 758 (2014)
5. M. Roos, S. Kielbassa, C. Schirling, T. Häring, J. Bansmann, R.J. Behm, *Rev. Sci. Instrum.* **78**, 084104 (2007)
6. K. Kohseinghaus, *Prog. Energy Combust. Sci.* **20**, 203 (1994)
7. A.C. Eckbreth, *Laser diagnostics for combustion temperature and species* (Taylor and Francis, New York, 1996)
8. M. Alden, J. Bood, Z. Li, M. Richter, *Proc. Combust. Inst.* **33**, 69 (2011)
9. J. Zetterberg, S. Blomberg, J. Zhou, J. Gustafson, E. Lundgren, in *Operando Research in Heterogeneous Catalysis* (Springer International Publishing, 2017), p. 131
10. E. Fridell, U. Westblom, M. Alden, A. Rosen, *J. Catal.* **128**, 92 (1991)
11. E. Fridell, A. Rosen, B. Kasemo, *Langmuir* **10**, 699 (1994)
12. E. Fridell, A.P. Elg, A. Rosén, B. Kasemo, *J. Chem. Phys.* **102**, 5827 (1995)
13. F. Gudmundson, J.L. Persson, M. Försth, F. Behrendt, B. Kasemo, A. Rosén, *J. Catal.* **179**, 420 (1998)
14. M. Försth, F. Gudmundson, J.L. Persson, A. Rosén, *Combust. Flame* **119**, 144 (1999)
15. F. Gudmundson, E. Fridell, A. Rosen, B. Kasemo, *J. Phys. Chem.* **97**, 12828 (1993)
16. W. Kang, O. Fujita, K. Ito, *J. Energy Res. Technol.* **118**, 82 (1996)
17. M. Reinke, J. Mantzaras, R. Bombach, S. Schenker, A. Inauen, *Combust. Flame* **141**, 448 (2005)
18. S. Eriksson, A. Schneider, J. Mantzaras, M. Wolf, S. Jaras, *Chem. Eng. Sci.* **62**, 3991 (2007)

19. J. Zetterberg, S. Blomberg, J. Gustafson, Z.W. Sun, Z.S. Li, E. Lundgren, M. Aldén, *Rev. Sci. Instrum.* **83** (2012)
20. S. Blomberg, C. Brackmann, J. Gustafson, M. Aldén, E. Lundgren, J. Zetterberg, *ACS Catal.* **2028** (2015)
21. J. Zetterberg, S. Blomberg, J. Gustafson, J. Evertsson, J. Zhou, E.C. Adams, P.-A. Carlsson, M. Aldén, E. Lundgren, *Nat Commun* **6** (2015)
22. S. Blomberg, J. Zetterberg, J. Gustafson, J. Zhou, C. Brackmann, E. Lundgren, *Topics in Catalysis*, **1** (2016)
23. S. Blomberg, J. Zhou, J. Gustafson, J. Zetterberg, E. Lundgren, *J. Phys. Condens. Matter* **28**, 453002 (2016)
24. S. Matera, S. Blomberg, M.J. Hoffmann, J. Zetterberg, J. Gustafson, E. Lundgren, K. Reuter, *ACS Catal.* **5**, 4514 (2015)
25. S. Blomberg, J. Zetterberg, J. Zhou, L.R. Merte, J. Gustafson, M. Shipilin, A. Trincherro, L.A. Miccio, A. Magaña, M. Ilyn, F. Schiller, J.E. Ortega, F. Bertram, H. Grönbeck, E. Lundgren, *ACS Catal.* (2016)
26. A. Zellner, R. Suntz, O. Deutschmann, *Angew Chem Int Ed Engl* **54**, 2653 (2015)
27. J. Haumann, J.M. Seitzman, R.K. Hanson, *Opt. Lett.* **11**, 776 (1986)
28. M. Aldén, S. Wallin, W. Wendt, *Appl. Phys. B* **33**, 205 (1984)
29. B.J. Kirby, R.K. Hanson, *Proc. Combust. Inst.* **28**, 253 (2000)
30. B.J. Kirby, R.K. Hanson, *Appl. Optics* **40**, 6136 (2001)
31. B.J. Kirby, R.K. Hanson, *Appl. Optics* **41**, 1190 (2002)
32. C.S. Goldenstein, V.A. Miller, R.K. Hanson, *Appl. Phys. B* **120**, 185 (2015)
33. Z.T. Alwahabi, J. Zetterberg, Z.S. Li, M. Aldén, *European Physical Journal D* **42**, 41 (2007)
34. G.W. Loge, J.J. Tice, F.B. Wampler, *J. Chem. Phys.* **79**, 196 (1983)
35. A.-L. Sahlberg, J. Kiefer, M. Aldén, Z. Li, *Appl Spectrosc* **70**, 1034 (2016)
36. C. Brackmann, J. Sjöholm, J. Rosell, M. Richter, J. Bood, M. Aldén, *Proc. Combust. Inst.* **34**, 3541 (2013)
37. T.B. Settersten, A. Dreizler, R.L. Farrow, *J. Chem. Phys.* **117**, 3173 (2002)